Journal of Zhejiang University-SCIENCE B (Biomedicine & Biotechnology) 2024 25(2):168-180
www.jzus.zju.edu.cn; www.springer.com/journal/11585
E-mail: jzus_b@zju.edu.cn

Research Article

https://doi.org/10.1631/jzus.B2300587

A proton birdcage coil integrated with interchangeable single loops for multi-nuclear MRI/MRS

Yi ZHANG[1,2,3*], Zhiyan QUAN[3,4*], Feiyang LOU[3,4,5], Yujiao FANG[6], Garth J. THOMPSON[6], Gao CHEN[1,2✉], Xiaotong ZHANG[1,2,3,4,5,7✉]

[1]*Department of Neurosurgery, the Second Affiliated Hospital, School of Medicine, Zhejiang University, Hangzhou 310009, China*
[2]*Key Laboratory of Precise Treatment and Clinical Translational Research of Neurological Diseases, Hangzhou 310009, China*
[3]*MOE Frontier Science Center for Brain Science and Brain-machine Integration, Zhejiang University, Hangzhou 310058, China*
[4]*Interdisciplinary Institute of Neuroscience and Technology, College of Biomedical Engineering & Instrument Science, Zhejiang University, Hangzhou 310027, China*
[5]*School of Medicine, Zhejiang University, Hangzhou 310020, China*
[6]*iHuman Institute, School of Life Science and Technology, ShanghaiTech University, Shanghai 201210, China*
[7]*College of Electrical Engineering, Zhejiang University, Hangzhou 310027, China*

Abstract: Energy metabolism is fundamental for life. It encompasses the utilization of carbohydrates, lipids, and proteins for internal processes, while aberrant energy metabolism is implicated in many diseases. In the present study, using three-dimensional (3D) printing from polycarbonate via fused deposition modeling, we propose a multi-nuclear radiofrequency (RF) coil design with integrated ^{1}H birdcage and interchangeable X-nuclei (^{2}H, ^{13}C, ^{23}Na, and ^{31}P) single-loop coils for magnetic resonance imaging (MRI)/magnetic resonance spectroscopy (MRS). The single-loop coil for each nucleus attaches to an arc bracket that slides unrestrictedly along the birdcage coil inner surface, enabling convenient switching among various nuclei and animal handling. Compared to a commercial ^{1}H birdcage coil, the proposed ^{1}H birdcage coil exhibited superior signal-excitation homogeneity and imaging signal-to-noise ratio (SNR). For X-nuclei study, prominent peaks in spectroscopy for phantom solutions showed excellent SNR, and the static and dynamic peaks of in vivo spectroscopy validated the efficacy of the coil design in structural imaging and energy metabolism detection simultaneously.

Key words: Energy metabolism; Magnetic resonance imaging (MRI); Magnetic resonance spectroscopy (MRS); Multi-nuclear; Radiofrequency coil; Three-dimensional (3D) printing

1 Introduction

Energy metabolism refers to pathways involving the utilization of carbohydrates, lipids, and proteins to supply fuel for biological functions, among which carbohydrates constitute 45% to 75% of the energy intake and consumption in humans (Elia and Cummings, 2007). As consistent energy supply is fundamental for life, aberrant energy metabolism is implicated not only in metabolic disorders such as obesity (Cani and Delzenne, 2009), diabetes (Scheuermann-Freestone et al., 2003), and mitochondrial myopathy (Milone and Wong, 2013), but also in common diseases including stroke (Robbins and Swanson, 2014), heart failure (Lopaschuk et al., 2021), cancer (Moreno-Sánchez et al., 2007), Alzheimer's disease (Ferreira et al., 2010), and others. The study of energy metabolism is therefore meaningful to provide clues for novel therapeutic strategies.

A key question in energy metabolism is how fuels are converted to the cellular energy carrier adenosine triphosphate (ATP) (Imamura et al., 2009), which has been studied in both clinical phenotype research and cutting-edge pre-clinical genotype experimentation.

✉ Gao CHEN, d-chengao@zju.edu.cn
Xiaotong ZHANG, zhangxiaotong@zju.edu.cn

* The two authors contributed equally to this work

Gao CHEN, https://orcid.org/0000-0003-1085-0028
Xiaotong ZHANG, https://orcid.org/0000-0002-9197-1421

Received Aug. 17, 2023; Revision accepted Nov. 8, 2023;
Crosschecked Jan. 8, 2024

Traditional in vitro methods are widely used due to their precision, while in vivo techniques provide real-time metabolic information (Hertz and Dienel, 2002). Positron emission tomography (PET) has the highest sensitivity among in vivo techniques, but the inherent radioactivity and complexity limit its applications (Magistretti and Allaman, 2015; Cherry et al., 2018). While magnetic resonance spectroscopy (MRS) is a promising alternative, its poor signal intensity remains a substantial challenge. Encouragingly, improved static magnetic field strength (B_0) and advanced radiofrequency (RF) systems have enabled major progress in MRS, including increased signal-to-noise ratio (SNR), sensitivity, and spectral resolution (Zhang et al., 2021).

In studying energy metabolism by MRS, X-nuclei (such as ^{2}H, ^{13}C, and ^{31}P) other than the commonly used ^{1}H can provide more metabolic flux information. ^{31}P has relatively high sensitivity (7% of ^{1}H) and 100% natural abundance, enabling its potential use in preclinical and clinical MRS (Kemp et al., 2007; Abdurrachim et al., 2017). Because each ATP molecule contains three phosphorus atoms, ^{31}P MRS has been extensively used to monitor ATP synthesis (Ren et al., 2015). To date, ^{13}C metabolic flux analysis has been considered the golden standard for precise in vitro and in vivo flux measurement (Gruetter et al., 2003; Long and Antoniewicz, 2019) by the tracing of carbon-based fuels. Also, ^{2}H MRS has recently emerged as a promising method for imaging glucose metabolism (de Feyter et al., 2018), overcoming the limitations of nonhyperpolarized ^{13}C MRS such as low sensitivity and complex spectroscopy (de Feyter and de Graaf, 2021).

In order to successfully perform metabolism detection, a multi-nuclear coil resonating at multiple frequencies is desired, but this is difficult to design due to mechanical and electrical challenges in achieving good performance at all frequencies. On the one hand, the ^{1}H signal is still necessary for both high-resolution anatomical imaging and higher-order B_0 shimming, because the gyromagnetic ratios (e.g., 10.7 MHz/T for ^{13}C, 6.5 MHz/T for ^{2}H, and 17.2 MHz/T for ^{31}P) and natural abundances (1.1% for ^{13}C and 0.0156% for ^{2}H) of X-nuclei are too low to achieve sufficient SNR for imaging and shimming. On the other hand, traps and positive-intrinsic-negative (PIN) diodes are commonly used to enable coil operation at multiple resonance frequencies (Mirkes et al., 2016; Choi et al., 2017; Ha et al., 2018), whereas the resulting power efficiency and coil SNR are inevitably degraded due to the additional electronic components. Although other configurations such as combinations of geometrically isolated double-tuned coil arrangements have been proposed without additional lossy elements, an expanded volume array is usually needed for a homogeneous B_1 field (pulsed RF magnetic field) and whole volume coverage (Augath et al., 2009; Alfonsetti et al., 2010). Recently, a multi-nuclear coil design was designed through numerical simulations, that is based on microstrips resonating at four frequencies, while experimental evaluations are still to be performed (Hernandez, 2021).

In this study, for the in vivo detection of energy metabolism, we provide a feasible and efficient solution for multi-nuclear MRS through devising a novel mechanical design of a multi-nuclear transmit/receive (TRx) coil. This comprises a ^{1}H birdcage TRx coil and interchangeable X-nuclei single-loop TRx coils for rodent magnetic resonance imaging (MRI)/MRS at 9.4 T. Through imaging experiments over saline phantoms and in vivo models, it is indicated that this design enables the acquisition of metabolic information from different nuclei, paving the way for more comprehensive studies on energy metabolism in vivo using MRS. Our work demonstrates the potential of the proposed coil for preclinical and translational research related to metabolism and its pathologies.

2 Materials and methods

2.1 Theory of energy detection in vivo by MRS

The theory of energy detection in vivo through multi-nuclear MRS relies on the resonance signal of X-nuclei (Fig. 1). For deuterium-based energy metabolism detection, the most prevalent mechanism and the positions of deuterium are shown. After oral intake or injection, deuterium-labeled glucose ([6,6'-$^2H_2$]-Glc) and important downstream metabolites ([3,3'-$^2H_2$]-lactate, [4-^{2}H] or [4,4'-$^2H_2$]-glutamate, [4-^{2}H] or [4,4'-$^2H_2$]-glutamine) can be detected through deuterium MRS. The in vivo ^{13}C experiment shares the same process but starts from [1-^{13}C]-acetate without glycolysis. ATP generated from glycolysis and citric acid circle can be detected through ^{31}P MRS.

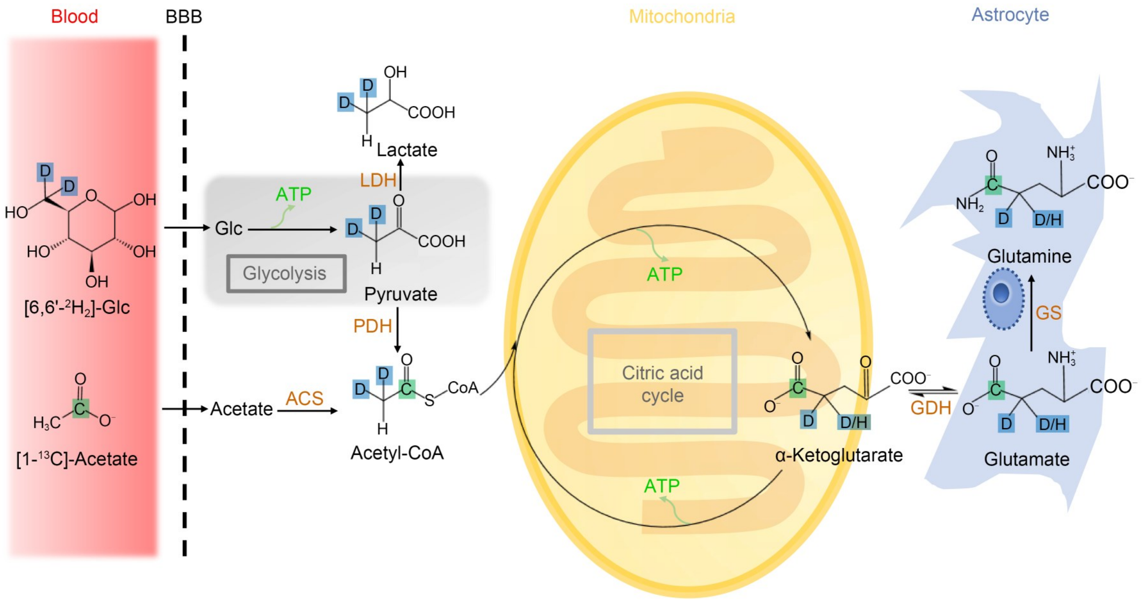

Fig. 1 Diagram of energy detection theory through multi-nuclear MRS. The metabolic pathways of [6,6'-$^2H_2$]-Glc and [1-^{13}C]-acetate are shown. The labeled isotopes are highlighted with blue boxes (^{2}H) and green boxes (^{13}C). MRS: magnetic resonance spectroscopy; D: deuterium; D/H: deuterium or hydrogen; C: ^{13}C; Glc, glucose; CoA: coenzyme A; ACS: acetal-CoA synthetase; ATP: adenosine triphosphate; BBB: blood–brain barrier; GDH: glutamate dehydrogenase; GS: glutamine synthetase; LDH: lactate dehydrogenase; PDH: pyruvate dehydrogenase.

2.2 Mechanical structure of multi-nuclear RF TRx coil

The multi-nuclear TRx coil is integrated with a ^{1}H birdcage TRx coil and interchangeable X-nuclei single loops. Fig. 2 shows the three-dimensional (3D) diagram and circuit schematics. In the field of magnetic resonance RF coils, the materials of coil shell themselves are not directly involved in the signal transmission and reception process. The principle of selecting materials is that they do not produce artifacts during imaging. Therefore, non-magnetic and non-eddy current high polymer materials are preferred. Mature options include polycarbonate (PC), fiberglass, and polyetheretherketone (PEEK) (Horch et al., 2010), among which PC has been widely used for small coils due to its economy and processability, while the latter two are more suitable for large coils. The PC used herein is LEXAN 920A from Sabic Innovative Plastics (Riyadh, Saudi Arabia), a medium viscosity flame retardant grade suitable for electrical applications. Its deflection temperature at 0.46 MPa is 135 °C (ISO 75/Be). The Vicat softening point is 141 °C (ISO 306); the hardness is 95.0 MPa (ISO 2039-1); the tensile strength at break is 60.0 MPa (ISO 527); the flexural yield strength is 90.0 MPa (ISO 178) (all standards from the International Organization for Standardization (ISO) can be queried on the official website: https://www.iso.org/standards.html). These properties are well above the imaging temperatures, providing adequate protection for the internal components while fixing the coil position. The volume resistivity is $>1.00\times 10^{15}\ \Omega\cdot\text{cm}$ (IEC 60093); the surface resistance is $>1.00\times 10^{15}\ \Omega$ (IEC 60093); the dielectric constant is 2.7 (IEC 60250) (all standards from the International Electrotechnical Commission (IEC) can be queried on the official website: https://webstore.iec.ch). Such PC cannot be magnetized or produce magnetically sensitive artifacts and has high RF penetration, maximizing signal transmission. Based on these properties, the coil housing was 3D-printed from this PC using fused deposition modeling (Fig. 2a). Two nested concentric cylinders were constructed: the inner cylinder has an outer diameter of about 75 mm; the outer cylinder has an inner diameter of about 111 mm; the PC thickness is about 3 mm; the total length is about 384 mm (see Fig. S1 for 3D printing details and Fig. S2 for 3D-printed structures). For this coil, the holder properties were assessed by electromagnetic interference, as demonstrated in the following experiments. A ^{1}H low-pass birdcage TRx coil was then constructed on the housing. The resonator components were on the inner cylinder's outer surface, and the shield was on its inner surface. Copper tapes (thickness: about 0.2 mm; width: about 25.0 mm) and tinned wires (diameter: about 1.8 mm) were used for rungs (rung length: about 138.0 mm) and end rings (ring diameter: about 75.0 mm) of the ^{1}H birdcage TRx coil. Fixed capacitors C_T (1.0 pF) and variable capacitors C_{T1} (1.0–12.0 pF) and C_{T2} (0.8–10.0 pF) were welded on each segment of the rungs to tune the birdcage TRx coil to 400.3 MHz (resonance frequency of ^{1}H at 9.4 T). Then, fixed capacitors C_{M1} (18.0 pF) and variable capacitors C_{M2} (0.8–10.0 pF) were added to compose a matching circuit. In addition, two fixed capacitors C (1000.0 pF) in the end rings were used to constrain the eddy currents caused by the wide copper tapes. For the best performance, capacitor adjustment rods were designed to link variable capacitors for tuning and matching (Fig. 2b). Finally, the ^{1}H birdcage TRx coil was tuned to 400.3 MHz and driven in quadrature mode.

Each X-nuclei single-loop TRx coil attaches to an arc bracket that slides freely along the inner surface of the inner cylinder, and they connect to the ^{1}H birdcage TRx coil through a quick mate (QMA) connector (Figs. 2c–2e). Tinned wires (diameter: about 1.8 mm) were used to form a ring (diameter: about 30.0 mm) with one or two turns. Fixed (C_{T3} and C_{M3}) and variable

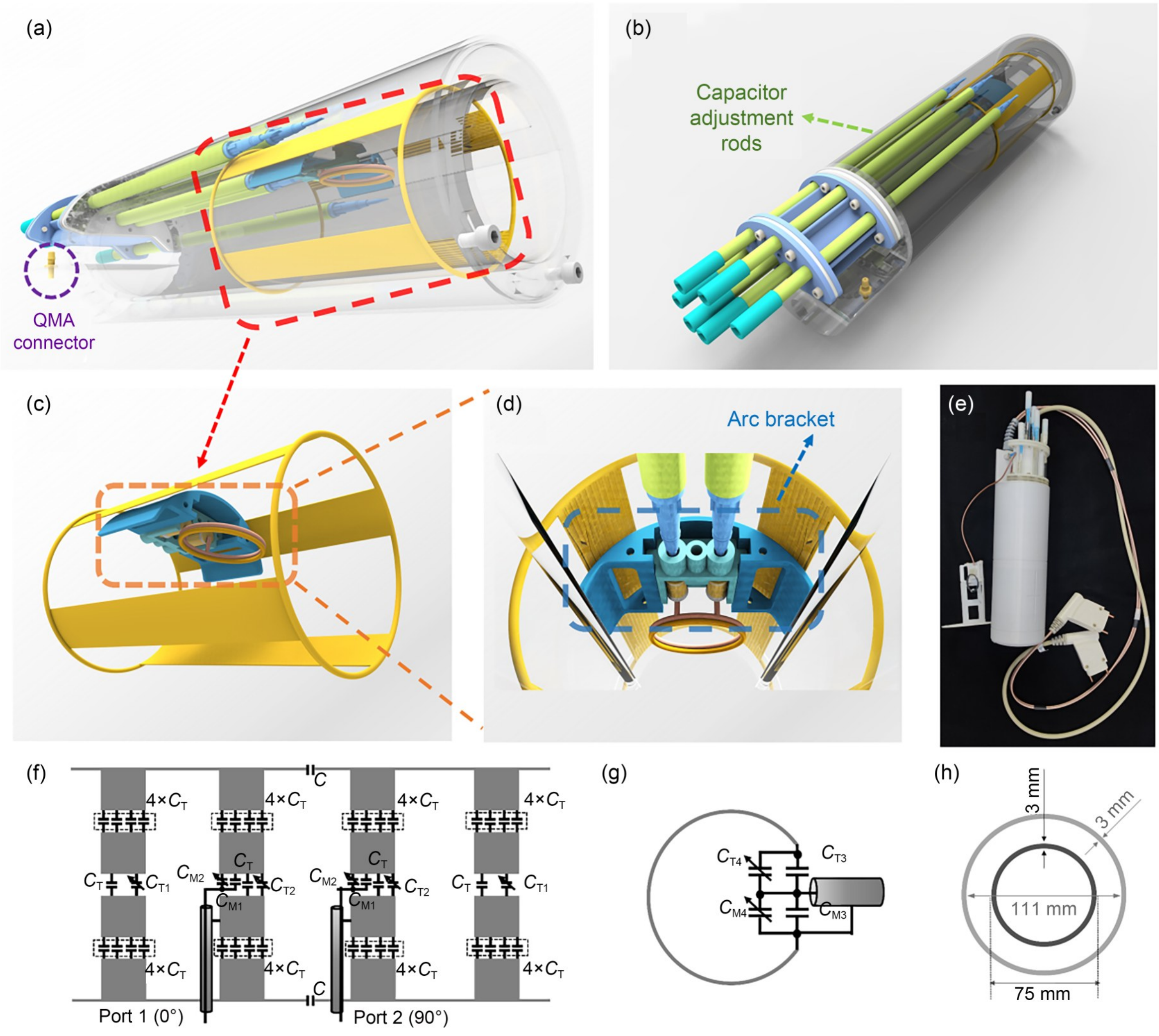

Fig. 2 Multi-nuclear TRx coil design. (a–e) Mechanical design of the proposed TRx coil. The ^{1}H birdcage TRx coil was fabricated on two nested concentric cylinders with single-loop TRx coils constructed on the arc bracket. Capacitor adjustment rods were designed to connect variable capacitors for tuning and matching. (f) Circuit schematic diagram of the ^{1}H TRx birdcage. (g) Circuit schematic diagram of the X-nuclei loop TRx coil. (h) Layout of cylinders showing diameter and thickness. TRx: transmit/receive; C_T: tuning capacitor; C_M: matching capacitor; QMA: quick mate.

(C_{T4} and C_{M4}) capacitors comprise the tuning and matching circuits, respectively. The circuits were placed on their housing with ^{1}H TRx coil driven in the quadrature mode and X-nuclei TRx coil driven in the linear mode (Figs. 2f–2h). In the present study, we fabricated three X-nuclei TRx coils for the following experiments to demonstrate the feasibility and flexibility of the design for multi-nuclear imaging of energy metabolism in vivo: ^{2}H at 61.4 MHz (C_{T3}: about 22.0 pF; C_{T4}: 1.0–12.0 pF; C_{M3}: about 330.0 pF; C_{M4}: 1.0–12.0 pF); ^{13}C at 100.6 MHz (C_{T3}: about 10.0 pF; C_{T4}: 1.5–40.0 pF; C_{M3}: about 200.0 pF; C_{M4}: 1.5–40.0 pF); ^{31}P at 162.0 MHz (C_{T3}: 0; C_{T4}: 1.5–40.0 pF; C_{M3}: about 56.0 pF; C_{M4}: 1.5–40.0 pF).

Installation rods allow fine tuning and matching during MRI in the mechanical design. Moreover, given that ^{23}Na has a similar gyromagnetic ratio to ^{13}C (11.3 MHz/T for ^{23}Na vs. 10.7 MHz/T for ^{13}C), we attempted to perform ^{23}Na MRI by slightly adjusting the variable capacitors of the ^{13}C TRx coil.

2.3 Phantom experiments

For different nuclei (^{1}H, ^{2}H, ^{13}C, ^{23}Na, and ^{31}P), we prepared five saline phantoms in 50 mL plastic centrifuge tubes (about 100 mm length, about 28 mm diameter). In detail, the ingredients of phantom solutions were as follows: (1) double-distilled water with 1 g/L $CuSO_4\cdot 5H_2O$ and 3 g/L NaCl (uniform ^{1}H phantom); (2) 99% (volume fraction) D_2O (deuterium oxide; Sigma-Aldrich, St. Louis, MO, USA) with 1 g/L $CuSO_4\cdot 5H_2O$ and 3 g/L NaCl (^{2}H phantom); (3) double-distilled water with 470.59 mL/L dimethylsulfoxide (DMSO; Sigma-Aldrich) and 3.6 g/L NaCl (^{13}C phantom referring to standard Bruker ^{13}C phantom T11596); (4) double-distilled water with 8.78 g/L (150 mmol/L) or 26.33 g/L (450 mmol/L) NaCl (^{23}Na phantom); (5) condensed Coca-Cola (^{31}P phantom (Medhurst et al., 2016)).

Experiments were carried out on a 9.4-T preclinical animal scanner (BioSpec 94/30 USR; Bruker BioSpin MRI, Ettlingen, Germany). A Bruker quadrature birdcage volume TRx coil (model T20204V3, Bruker BioSpin MRI) with 72 mm inner diameter was selected as a reference for ^{1}H imaging comparison. Data were acquired from different phantoms based on the coil nucleus type. The sequences and parameters are summarized in Table 1.

2.4 In vivo experiments

C57 mice (*n*=3; Zhejiang Academy of Medical Sciences, Hangzhou, China) were used in this study. Through the scanning, each mouse was anesthetized by 1%–3% (volume fraction) isoflurane mixed with compressed air (1.5 L/min). The body temperature was maintained at 37 °C and the respiratory rate was monitored. For ^{2}H MRS, the mice were intraperitoneally injected with [6,6'-$^2H_2$]-glucose (Sigma-Aldrich; 2 g/kg body mass with concentration 1 mol/L). After 10 min, a series of spectroscopy sessions were preformed consecutively in the brain through pulse-acquired sequence with the outer volume suppression (OVS) module. For ^{13}C MRS, the procedure was the same but injected with [1-^{13}C]-acetate (Sigma-Aldrich; 2 g/kg body mass with concentration 3 mol/L). For ^{31}P MRS, the data were attained without any injection. The sequences and parameters are summarized in Table 2.

Table 1 Sequences and parameters used in phantoms

Nucleus	Sequence	TR (ms)	TE (ms)	FA (°)	BW (Hz/pixel)	Slice thickness (mm)	Matrix size	FOV (mm^2)	Average times
^{1}H/^{2}H	ADJ_B1MAP	6.6	2.0	20		3	80×80	40×40	1
	Localizer	100.0	2.3	30		3	160×160	40×40	2
	ADJ_B1MAP	6.4	2.0	60		5	62×32	135.6×32.0	10
^{23}Na	QA_SNR	100.0	15.0	90 (excitation) 180 (refocusing)		5	40×40	40×40	20
	T1_FLASH	66.0	2.3	60		5	32×32	32×32	200
^{13}C	Pulse acquired	1000.0		45	1.22				100
^{31}P	Pulse acquired	1000.0		30	1.02				100

TR: repetition time; TE: echo time; FA: flip angle; BW: bandwidth; FOV: field of view.

Table 2 Sequences and parameters used in vivo

Nucleus	Sequence	TR (ms)	TE (ms)	FA (°)	BW (Hz/pixel)	Slice thickness (mm)	Matrix size	FOV (mm^2)	Average times	Turbo factor
^{1}H	T1_FLASH	350	2.50	25		1	160×80	80×40	4	
	T2_TurboRARE	800	6.25	90 (excitation) 180 (refocusing)		1	240×120	80×40	8	6
^{2}H	Pulse acquired	1000		30	2.00				300	
^{13}C	Pulse acquired	1068		45	1.25				600	
^{31}P	Pulse acquired	1148		30	1.13				1000	

TR: repetition time; TE: echo time; FA: flip angle; BW: bandwidth; FOV: field of view.

2.5 Data analysis

The transmission efficiency of the RF TRx coil was evaluated by obtaining a B_1^+ map, which measures the amplitude of the circularly polarized component of pulsed RF magnetic field (Nehrke and Börnert, 2012). Given that B_1^+ is proportional to the driving voltage that is in turn proportional to the square root of power, the transmission efficiency was expressed in Hz (or μT, for B_1^+) per square root of watt (Hz/W$^{1/2}$). The normalized mean and standard deviation of B_1^+ were computed in MATLAB (the Mathworks, Natick, MA, USA) to determine the B_1^+ homogeneity. The SNR, defined as the ratio of the mean magnetic resonance image signal intensity of the region of interest (ROI) (the red circles shown in Figs. 3d–3f) to the standard deviation of the background signal intensity (the orange boxes shown in Figs. 3d–3f), was calculated in MATLAB. The MRS data were all analyzed using TopSpin 4.2.0 software (Bruker Biospin, Rheinstetten, Germany).

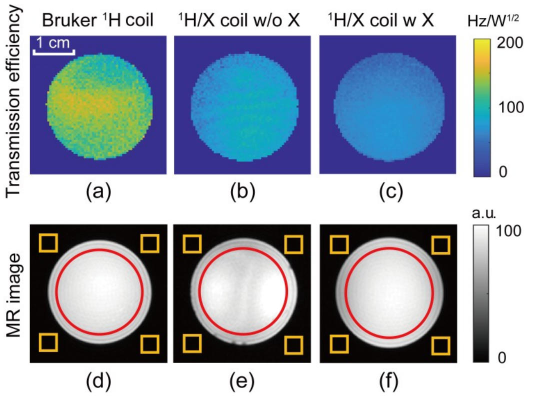

Fig. 3 Transmission performance (a–c) and SNR (d–f) comparison on ^{1}H phantom among the Bruker ^{1}H birdcage TRx coils and the custom-made ^{1}H birdcage TRx coils with/without an X-nuclei single-loop TRx coil inserted. The mean and standard deviation of B_1^+ efficiency were calculated to demonstrate the transmission efficiency and homogeneity of the TRx coils ((a) (128.26±16.64) Hz/W$^{1/2}$; (b) (80.00±10.87) Hz/W$^{1/2}$; (c) (62.30±8.04) Hz/W$^{1/2}$). The SNR was computed as the mean signal intensity within the red circles divided by the standard deviation within the orange boxes ((d) about 129; (e) about 162; (f) about 169). SNR: signal-to-noise ratio; TRx: transmit/receive; w/o: without; w: with; X: X-nuclei single-loop TRx coil; MR: magnetic resonance; a.u.: arbitrary unit.

3 Results

3.1 Performance of ^{1}H TRx coil

The evaluation of transmit efficiency is depicted in Figs. 3a–3c. We compared the custom-made ^{1}H TRx coil with or without X-nuclei single-loop TRx coil to the Bruker ^{1}H birdcage TRx coil. Apparently, the transmission performance of the latter (around 120 Hz/W$^{1/2}$) was better than that of the custom-built ^{1}H TRx coil with (around 60 Hz/W$^{1/2}$) and without (around 80 Hz/W$^{1/2}$) the X-nuclei single loop. Influenced by the elements of single loop, the transmit efficiency of custom-made ^{1}H TRx coil decreased when they were combined. Regarding the homogeneity of B_1^+ efficiency, the custom-made ^{1}H TRx coil exhibited better homogeneity both with (about 8.04 Hz/W$^{1/2}$) and without (about 10.87 Hz/W$^{1/2}$) single loop, compared to the Bruker ^{1}H TRx coil (about 16.64 Hz/W$^{1/2}$). The axial plane of ^{1}H phantom magnetic resonance image is shown in Figs. 3d–3f with the SNR calculated. The SNR of Bruker ^{1}H TRx coil (about 129) was about 76% of custom-made ^{1}H TRx coil with singe loop (about 169) and 80% of the one without single loop (about 162).

The custom-made ^{1}H TRx coil was designed for high-resolution structure imaging and higher-order shimming during performing energy metabolism detection; therefore, T1-weighted images and T2-weighted images were acquired in vivo through "T1_FLASH" and "T2_TurboRARE" sequences, respectively (Fig. 4), with the X-nuclei single-loop TRx coil inserted. The borders of organs (red lines) can be readily delineated from the structural images, which adequately satisfies the requirements of energy metabolism detection in specific organs.

3.2 Performance of ^{2}H TRx coil

Despite the gyromagnetic ratio of deuterium being only 1/7–1/6 of hydrogen (6.5 MHz/T vs. 42.6 MHz/T), transmission performance evaluation and MRI could be successfully performed using 99% D_2O phantom (Figs. 5a and 5b). Both the B_1^+ efficiency and magnetic resonance image through deuterium phantom demonstrated the excellent performance of ^{2}H single-loop TRx coil, with the transmission efficiency and signal intensity decreasing substantially along the direction perpendicular to the coil surface. Given that the diameter of ^{2}H single-loop TRx coil is 30 mm and that of the phantom is 28 mm, the upper half of the signal in the phantom was acquired (Fig. 5b). For the in vivo experiments, the mouse brain was selected as the ROI 10 min following [6,6'-$^2H_2$]-Glc injection (red box in Fig. 5c). Through a series of deuterium MRS acquisitions, changes in the concentrations of deuterium-labeled metabolites were observed. For quantitative analysis, spectrum fitting and integration were performed (Fig. S3). While [6,6'-$^2H_2$]-Glc continued to participate in oxidative phosphorylation, the concentration of original glucose decreased (the integration area changed from 508 to 451, 345, 324, and 266 over

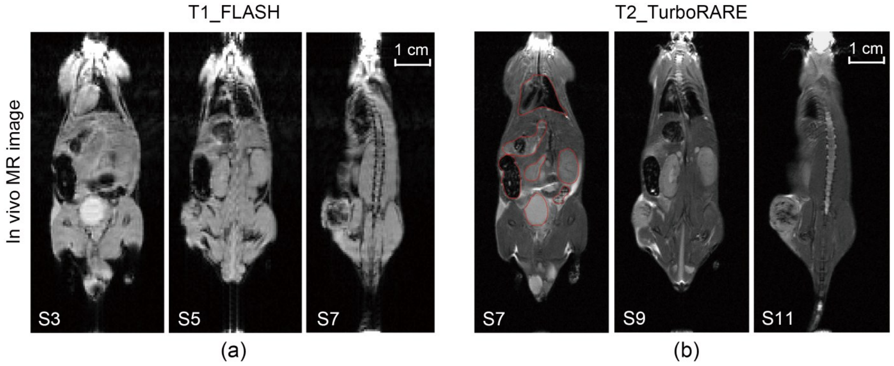

Fig. 4 T1-weighted (a) and T2-weighted (b) whole-body images of mouse using a custom-made ^{1}H birdcage TRx coil. S3, S5, S7, S9, and S11 denote the slice numbers. TRx: transmit/receive; MR: magnetic resonance.

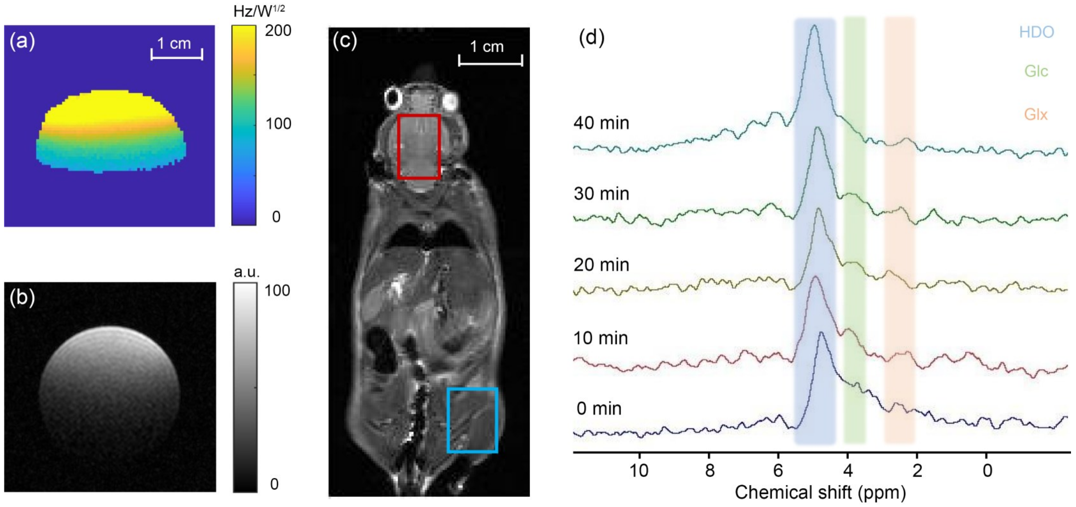

Fig. 5 Performance of ^{2}H TRx coil. (a) Transmission performance of the ^{2}H loop TRx coil. (b) MR image of 99% D_2O phantom. (c) ROI of MRS in mouse (red box: ROI of ^{2}H and ^{13}C experiment; blue box: ROI of ^{31}P experiment). (d) Time series of deuterium MRS acquired in the mouse brain post-injection (0, 10, 20, 30, and 40 min time points after scanning onset). TRx: transmit/receive; MR: magnetic resonance; D_2O: deuterium oxide; ROI: region of interest; MRS: magnetic resonance spectroscopy; HDO: semi-heavy water molecule consists of one hydrogen, one deuterium, and one oxygen; Glc: glucose; Glx: glutamate and glutamine; ppm: parts per million (×10^{-6}); a.u.: arbitrary unit.

time), resulting in a ratio range of 0.52 to 1.00 relative to the initial concentration. In contrast, the end metabolite HDO (semi-heavy water molecule consists of one hydrogen, one deuterium, and one oxygen) steadily increased from 734 to 736, 788, 826, and 1045. The concentrations of glutamate and glutamine (Glx; their chemical shifts are too close to distinguish) fluctuated among 144 (0 min), 200 (10 min), 203 (20 min), 172 (30 min), and 126 (40 min) (Fig. 5d).

3.3 Performance of other X-nuclei TRx coils

Since no phantoms like H_2O or 99% D_2O were available for ^{13}C or ^{31}P, spectroscopy data from both phantoms and mice were obtained to confirm the viability of ^{13}C and ^{31}P single-loop TRx coils. The prominent peaks in spectroscopy from both ^{31}P (Fig. 6a) and ^{13}C (Fig. 6b) phantoms demonstrated satisfying SNR. The ^{13}C spectroscopy peak split into four peaks due to the scalar coupling of two ^{13}C atoms in DMSO. As ^{31}P spectroscopy primarily detects energy metabolism in the muscle and liver, the mouse thigh was chosen as the ROI for static in vivo ^{31}P MRS (blue box in Fig. 5c). Due to the natural abundance of ^{31}P, phosphocreatine (PCr) was evident as the internal ^{31}P spectroscopy reference, and ATP peaks were also identifiable (Fig. 6c). For in vivo ^{13}C experiments, animal and scanning procedures were identical to ^2H. Through a series of ^{13}C MRS acquisitions, the integration area of [1-^{13}C]-acetate first increased and then decreased with ratios relative to 0 min of 1.08 (10 min), 1.24 (20 min), 1.15 (30 min), and 0.77 (40 min). Similarly, the ratios for [5-^{13}C]-glutamine were 1.03 (10 min), 1.48 (20 min), 1.35 (30 min), and 0.85 (40 min) (Fig. 6d).

After tuning the ^{13}C single-loop TRx coil resonance frequency to coincide with the ^{23}Na resonance frequency (105.9 MHz), we made an attempt to acquire ^{23}Na MRI. The transmission efficiency was circa 160–190 Hz/W$^{1/2}$ in 450 mmol/L NaCl solutions (Fig. S4a). Magnetic resonance images could be gathered but with relative low SNR (circa 10–20, Fig. S4b). The signal attenuation could be observed along the direction perpendicular to the ^{23}Na surface TRx coil in the T1-weighted image on 150 mmol/L NaCl solutions (Fig. S4c).

4 Discussion

Energy metabolism depends on the conversion of nutrients, that is, mainly of carbohydrates, lipids and proteins. Abnormal energy metabolism (e.g., impaired energy utilization, changes in nutrient preferences,

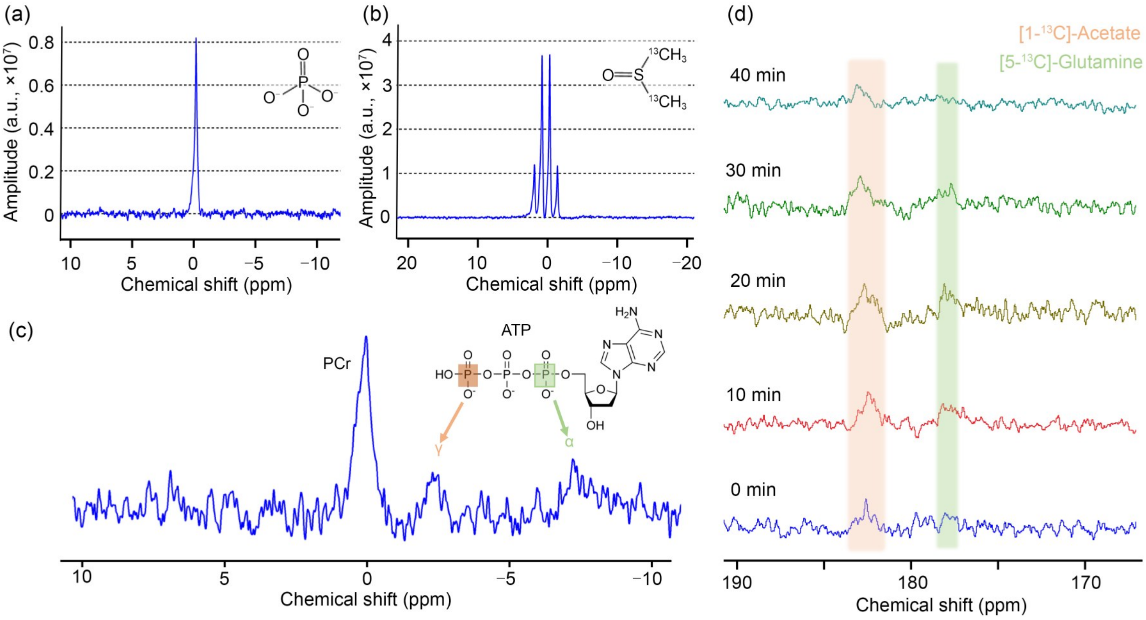

Fig. 6 Performance of ^{31}P and ^{13}C TRx coils. (a) ^{31}P spectroscopy of phantom. (b) ^{13}C spectroscopy of phantom. (c) Static ^{31}P spectroscopy over the mouse thigh with natural abundance. (d) Time series of ^{13}C MRS acquired in the mouse brain post-injection (at time points of 0, 10, 20, 30, and 40 min after scanning onset). TRx: transmit/receive; MRS: magnetic resonance spectroscopy; ATP: adenosine triphosphate; PCr: phosphocreatine; ppm: parts per million (×10^{-6}); a.u.: arbitrary unit.

and adjustments in metabolic pathways) occurs in many disorders, rendering the detection of energy metabolism a meaningful approach to explore pathological mechanisms, aid in disease diagnosis, and implement personalized treatment programs. While ex vivo sample analysis (e.g., cerebrospinal fluid (Weiss et al., 2016), peripheral blood (Al-Mosalem et al., 2009), and tissues (Beyoğlu et al., 2013)) provides accurate quantitative results, in vivo methods are also essential sources of invaluable real-time metabolic flux data, especially when samples are difficult to obtain such as those from the brain (Hertz and Dienel, 2002). For in vivo energy metabolism detection, we propose a novel mechanical design of a multi-nuclear TRx coil. Through an interchangeable arc bracket holding an X-nuclei single loop, we integrated the multi-nuclei TRx coil with a ^{1}H birdcage TRx coil for a small animal (mouse) at 9.4 T, with the resonance frequency easily switched for X-nuclei signal detection to meet various research demands.

Compared to the Bruker ^{1}H birdcage TRx coil, the proposed ^{1}H birdcage TRx coil shows lower transmission efficiency but higher SNR, which may result from the wider rung design enabling smaller conduction currents during transmission and lower coil loss during reception. Moreover, the custom-made ^{1}H TRx coil exhibits better B_1^+ uniformity, consistent with our previous work (Zhang et al., 2022). The coupling of the custom-made ^{1}H birdcage TRx coil and the X-nuclei single-loop TRx coils is effectively reduced by the spacing between them as well as due to relatively large differences in their resonating frequencies (1/7–1/4 as of ^{1}H), as evidenced by the negligible interference induced in anatomical images when an X-nuclei TRx coil was inserted. The outcome of electromagnetic simulations further shows that the coupling between the ^{1}H birdcage coil and the X-nuclei surface coil is considered negligible or trivial (Fig. S5 and Table S1).

Although ^{13}C metabolic flux analysis has been extensively used for flux quantification in vitro and in vivo (Gruetter et al., 2003; Long and Antoniewicz, 2019), non-hyperpolarized ^{13}C MRS is partly limited by poor sensitivity and spatial resolution (Rothman et al., 2019), whereas hyperpolarized ^{13}C MRS has demanding facility requirements under in vivo application (von Morze et al., 2021). In contrast, deuterium MRS has shown promising advantages due to favorable T1/T2 ratios, enabling additional signal averaging to improve ^{2}H MRS sensitivity (de Feyter and de Graaf, 2021). While ^{2}H MRS applications remain viable based on carbohydrates (mainly glucose and acetate), ^{2}H MRS has successfully distinguished gliomas from normal brain tissue based on the Warburg effect (tumor cells exhibit increased glucose uptake and unusually high glycolysis rates, producing substantial lactate accumulation, whereas normal cells prefer aerobic oxidation) (Warburg, 1956). Moreover, ^{2}H MRS possesses the potential to link microscale genotypic changes to macroscale phenotypic changes through in vivo methods (Batsios et al., 2022; Taglang et al., 2022). Herein, the ^{2}H TRx coil exhibited good transmit efficiency and SNR in phantoms as a surface coil, even if the gyromagnetic ratio of ^{2}H was only 1/7–1/6 of ^{1}H. A mathematical model established in isoflurane-anesthetized mice determined a cerebral glucose consumption rate of (0.28±0.13) μmol/(g·min) and a tricarboxylic acid cycle flux of (0.6±0.2) μmol/(g·min) using ^{2}H MRS (Lu et al., 2017). Based on our experimental data and scanning time, the glucose ratio should range from 0.55 to 1.00, and the Glx concentration should first increase and then decrease. The results from ^{2}H MRS of a mouse brain showed similar time-varying integration areas for HDO, glucose, and Glx, verifying the feasibility and reliability of the ^{2}H single-loop TRx coil. Notably, oxidative phosphorylation was the primary energy source in this healthy mouse; thus, no substantial lactate accumulation peaks were observed.

The pronounced peaks observed in ^{31}P and ^{13}C phantom spectroscopy demonstrated the excellent SNRs of the ^{31}P and ^{13}C coils. Glycogen is a branched glucose polymer that acts as a glucose reservoir, involving high-energy phosphates in covalent phosphorylation and allosteric ligand binding processes (Roach, 2002). As the two largest glycogen stores, the liver and skeletal muscle are widely taken as target organs in ^{31}P MRS research (Valkovič et al., 2017). In this study, we selected the mouse thigh to demonstrate natural ^{31}P abundance, and both the internal reference PCr and energy currency ATP were readily detected, meeting most ^{31}P MRS requirements. For in vivo ^{13}C MRS, following conversion to acetal-CoA, the metabolic process was the same as for ^{2}H MRS; thus, a comparable tendency was noted. However, the substrates [6,6'-^{2}H$_2$]-glucose and [1-^{13}C]-acetate differed: the former showed a steady decline, whereas the latter initially elevated and then dropped, despite that scanning was started at the same time. This phenomenon mainly resulted from the higher glucose transport and use rates than acetate (Deelchand et al., 2009; Mergenthaler et al., 2013), causing the glucose peak to precede the acetate peak.

While the sodium–potassium pump (sodium–potassium adenosine triphosphatase) appears to associate ^{23}Na with ATP, no study has yet explored the underlying energy metabolism value of ^{23}Na. The relatively high sensitivity of ^{23}Na enables performing ^{23}Na MRI. Typically, ^{23}Na MRI applications rely on changes in intracellular and extracellular sodium concentrations when cells die or experience functional degeneration. Successful applications include the detection of cartilage degeneration (Shapiro et al., 2000), the monitoring of tumor therapy response (James et al., 2010), and the evaluation of stroke conditions (O'Donnell et al., 2013). Because the resonance frequencies of ^{13}C and ^{23}Na are quite close, we attempted to acquire ^{23}Na MRI by adjusting the rods and slightly shifting the resonating frequency. Although the B_1^+ efficiency and SNR were suboptimal, T1-weighted images were successfully obtained by increasing the number of averages.

Achieving optimal SNR while enabling flexible nucleus switching presents tradeoffs in multinuclear coil design, since commonly used traps and PIN diodes will degrade the SNR. Gareis et al. (2006) raised single-tuned surface phased array coils, achieving significant SNR over birdcage coils of the same diameter. However, the coil exchanging procedure requires the movement of anaesthetized animals, which may result directly in altered animal position, thus bringing in registration issues or degradation of the static shim. The birdcage coil design proposed by Choi et al. (2016) consisting of six swappable birdcage coils skillfully resolved this problem without SNR loss since each coil is single-tuned; however, the separation of ^{1}H and X-nuclei coils causes inconvenience when adjusting ROIs in vivo (e.g., a tumor mice experiment may need localized spectra in both ipsilateral tumor side and the same contralateral healthy side, which demands shimming twice in two different ROIs, prompting the need for another exchanging procedure of ^{1}H coil). Our combined design (a birdcage coil for ^{1}H and interchangeable surface coils for X-nuclei without traps or PIN diodes) handles the issues of animal disturbance caused by the coil exchanging procedure while modifying the ROI in a potential animal experiment (Video S1). Because of additional electronic elements, the B_1 homogeneity and RF power calibration of volume coil were slightly influenced (Fig. 3), which was relatively acceptable for the experiments. In addition, constrained by the inherent drawbacks of surface coils, the B_1 homogeneity and RF power calibration of our surface coil are inferior to the multinuclear volume coils designed by Choi et al. (2016), whereas its performance is relatively decent in the regions close to the surface coil.

Overall, our mechanical multi-nuclear TRx coil design can meet the needs of both structural imaging and energy metabolism detection. Although such a design may suit relatively small ROIs and superficial areas, designing a separate-volume TRx coil for X-nuclei excitation (providing more uniform B_1^+) and a surface TRx coil for signal reception (allowing higher sensitivity) could produce better results in X-nuclei studies. Nonetheless, incorporating another TRx coil to enlarge the total imaging capacity to additional nucleus in this scenario is likely to be difficult. The present design offers substantial flexibility to conduct MRI/MRS for any X-nuclei alongside with ^{1}H. Potential future enhancements could explore metamaterials as an alternative TRx coil construction technique to improve the B_1 and SNR of the X-nuclei signals (Choi et al., 2020).

5 Conclusions

In the present study, we proposed an innovative mechanical multi-nuclear TRx coil design. Specifically, the coil housing was 3D-printed from PC using fused deposition modeling to comprise a ^{1}H birdcage TRx coil and interchangeable X-nuclei single-loop TRx coils (^{2}H, ^{13}C, and ^{31}P). The X-nuclei single loop attaches to an arc bracket that slides along the coil inner surface, allowing convenient switching between any nucleus according to the research objective. Adjustment tuning rods were designed to connect variable capacitors for circuitry tuning and matching. The coil performance in both structural imaging and energy metabolism detection was validated through phantom saline and in vivo model experiments, demonstrating its capability to facilitate well-executed research on energy metabolism detection using multi-nuclear MRS.

Data availability statement

The data presented in this study are available from the corresponding author upon reasonable request.

Acknowledgments

This work was supported in part by the STI 2030–Major Projects (No. 2021ZD0200401), the National Key Research and Development Program of China (No. 2018YFA0701400), the National Natural Science Foundation of China (Nos. 52277232, 52293424, 81701774, and 61771423), the Fundamental Research Funds for the Central Universities (Nos. 226-2022-00136 and 226-2023-00125), the Zhejiang Provincial Natural Science Foundation of China (No. LR23E070001), the Key R&D Program of Jiangsu Province (No. BE2022049), and the Key-Area R&D Program of Guangdong Province (No. 2018B030333001), China.

Author contributions

Yi ZHANG, Zhiyan QUAN, and Xiaotong ZHANG designed the study. Garth J. THOMPSON provided experimental instrument and instructions on MRI operation. Yi ZHANG, Zhiyan QUAN, Feiyang LOU, Yujiao FANG, and Xiaotong ZHANG performed the experiments and collected data. Yi ZHANG and Zhiyan QUAN analyzed the data. Yi ZHANG and Zhiyan QUAN wrote the draft. Xiaotong ZHANG and Gao CHEN supervised the study and obtained the funding. All authors have read and approved the final manuscript, and therefore, have full access to all the data in the study and take responsibility for the integrity and security of the data.

Compliance with ethics guidelines

Yi ZHANG, Zhiyan QUAN, Feiyang LOU, Yujiao FANG, Garth J. THOMPSON, Gao CHEN, and Xiaotong ZHANG declare that there is no conflict of interest.

All institutional and national guidelines for the care and use of laboratory animals were followed. Animal experimentation was approved by the Ethics Committee of Laboratory Animal Center of Zhejiang University (approval number: ZJU20200064).

References

Abdurrachim D, Nabben M, Hoerr V, et al., 2017. Diabetic *db*/*db* mice do not develop heart failure upon pressure overload: a longitudinal *in vivo* PET, MRI, and MRS study on cardiac metabolic, structural, and functional adaptations. *Cardiovasc Res*, 113(10):1148-1160. https://doi.org/10.1093/cvr/cvx100

Alfonsetti M, Sotgiu A, Alecci M, 2010. Design and testing of a 1.5 Tesla double-tuned (^{1}H/^{31}P) RF surface coil with intrinsic geometric isolation. *Measurement*, 43(9):1266-1276. https://doi.org/10.1016/j.measurement.2010.07.003

Al-Mosalem OA, El-Ansary A, Attas O, et al., 2009. Metabolic biomarkers related to energy metabolism in Saudi autistic children. *Clin Biochem*, 42(10-11):949-957. https://doi.org/10.1016/j.clinbiochem.2009.04.006

Augath M, Heiler P, Kirsch S, et al., 2009. *In vivo* ^{39}K, ^{23}Na and ^{1}H MR imaging using a triple resonant RF coil setup. *J Magn Reson*, 200(1):134-136. https://doi.org/10.1016/j.jmr.2009.05.005

Batsios G, Taglang C, Tran M, et al., 2022. Deuterium metabolic imaging reports on TERT expression and early response to therapy in cancer. *Clin Cancer Res*, 28(16):3526-3536. https://doi.org/10.1158/1078-0432.CCR-21-4418

Beyoğlu D, Imbeaud S, Maurhofer O, et al., 2013. Tissue metabolomics of hepatocellular carcinoma: tumor energy metabolism and the role of transcriptomic classification. *Hepatology*, 58(1):229-238. https://doi.org/10.1002/hep.26350

Cani PD, Delzenne NM, 2009. The role of the gut microbiota in energy metabolism and metabolic disease. *Curr Pharm Des*, 15(13):1546-1558. https://doi.org/10.2174/138161209788168164

Cherry SR, Jones T, Karp JS, et al., 2018. Total-body PET: maximizing sensitivity to create new opportunities for clinical research and patient care. *J Nucl Med*, 59(1):3-12. https://doi.org/10.2967/jnumed.116.184028

Choi CH, Ha Y, Veeraiah P, et al., 2016. Design and implementation of a simple multinuclear MRI system for ultra high-field imaging of animals. *J Magn Reson*, 273:28-32. https://doi.org/10.1016/j.jmr.2016.10.007

Choi CH, Hong SM, Ha Y, et al., 2017. Design and construction of a novel ^{1}H/^{19}F double-tuned coil system using PIN-diode switches at 9.4T. *J Magn Reson*, 279:11-15. https://doi.org/10.1016/j.jmr.2017.04.005

Choi CH, Hong SM, Felder J, et al., 2020. The state-of-the-art and emerging design approaches of double-tuned RF coils for X-nuclei, brain MR imaging and spectroscopy: a review. *Magn Reson Imaging*, 72:103-116. https://doi.org/10.1016/j.mri.2020.07.003

Deelchand DK, Shestov AA, Koski DM, et al., 2009. Acetate transport and utilization in the rat brain. *J Neurochem*, 109(Suppl 1):46-54. https://doi.org/10.1111/j.1471-4159.2009.05895.x

de Feyter HM, de Graaf RA, 2021. Deuterium metabolic imaging – Back to the future. *J Magn Reson*, 326:106932. https://doi.org/10.1016/j.jmr.2021.106932

de Feyter HM, Behar KL, Corbin ZA, et al., 2018. Deuterium metabolic imaging (DMI) for MRI-based 3D mapping of metabolism in vivo. *Sci Adv*, 4(8):eaat7314. https://doi.org/10.1126/sciadv.aat7314

Elia M, Cummings JH, 2007. Physiological aspects of energy metabolism and gastrointestinal effects of carbohydrates. *Eur J Clin Nutr*, 61:S40-S74. https://doi.org/10.1038/sj.ejcn.1602938

Ferreira IL, Resende R, Ferreiro E, et al., 2010. Multiple defects in energy metabolism in Alzheimers disease. *Curr Drug Targets*, 11(10):1193-1206. https://doi.org/10.2174/1389450111007011193

Gareis D, Neuberger T, Behr VC, et al., 2006. Transmit-receive coil-arrays at 17.6T, configurations for ^{1}H, ^{23}Na, and ^{31}P MRI. *Concepts Magn Reson Part B Magn Reson*

Eng, 29B(1):20-27.
https://doi.org/10.1002/cmr.b.20055

Gruetter R, Adriany G, Choi IY, et al., 2003. Localized *in vivo* ^{13}C NMR spectroscopy of the brain. *NMR Biomed*, 16(6-7): 313-338.
https://doi.org/10.1002/nbm.841

Ha Y, Choi CH, Shah NJ, 2018. Development and implementation of a PIN-diode controlled, quadrature-enhanced, double-tuned RF coil for sodium MRI. *IEEE Trans Med Imaging*, 37(7):1626-1631.
https://doi.org/10.1109/TMI.2017.2786466

Hernandez D, 2021. Design of a coplanar interlayer gapped microstrips arrangement for multi-nuclei (^{1}H, ^{19}F, ^{31}P, and ^{23}Na) applications in 7T MRI. *Appl Sci*, 11(3):957.
https://doi.org/10.3390/app11030957

Hertz L, Dienel GA, 2002. Energy metabolism in the brain. *Int Rev Neurobiol*, 51:1-102, IN1-IN4.
https://doi.org/10.1016/s0074-7742(02)51003-5

Horch RA, Wilkens K, Gochberg DF, et al., 2010. RF coil considerations for short-T_2 MRI. *Magn Reson Med*, 64(6): 1652-1657.
https://doi.org/10.1002/mrm.22558

Imamura H, Nhat KPH, Togawa H, et al., 2009. Visualization of ATP levels inside single living cells with fluorescence resonance energy transfer-based genetically encoded indicators. *Proc Natl Acad Sci USA*, 106(37):15651-15656.
https://doi.org/10.1073/pnas.0904764106

James JR, Gao Y, Soon VC, et al., 2010. Controlled radiofrequency hyperthermia using an MR scanner and simultaneous monitoring of temperature and therapy response by ^{1}H, ^{23}Na and ^{31}P magnetic resonance spectroscopy in subcutaneously implanted 9L-gliosarcoma. *Int J Hyperthermia*, 26(1):79-90.
https://doi.org/10.3109/02656730903373509

Kemp GJ, Meyerspeer M, Moser E, 2007. Absolute quantification of phosphorus metabolite concentrations in human muscle *in vivo* by ^{31}P MRS: a quantitative review. *NMR Biomed*, 20(6):555-565.
https://doi.org/10.1002/nbm.1192

Long CP, Antoniewicz MR, 2019. High-resolution ^{13}C metabolic flux analysis. *Nat Protoc*, 14(10):2856-2877.
https://doi.org/10.1038/s41596-019-0204-0

Lopaschuk GD, Karwi QG, Tian R, et al., 2021. Cardiac energy metabolism in heart failure. *Circ Res*, 128(10):1487-1513.
https://doi.org/10.1161/CIRCRESAHA.121.318241

Lu M, Zhu XH, Zhang Y, et al., 2017. Quantitative assessment of brain glucose metabolic rates using in vivo deuterium magnetic resonance spectroscopy. *J Cereb Blood Flow Metab*, 37(11):3518-3530.
https://doi.org/10.1177/0271678X17706444

Magistretti PJ, Allaman I, 2015. A cellular perspective on brain energy metabolism and functional imaging. *Neuron*, 86(4): 883-901.
https://doi.org/10.1016/j.neuron.2015.03.035

Medhurst L, Shahnaz F, Ramnarine N, et al., 2016. Measurement of phosphates in soft drinks: a general chemistry experiment using NMR. *In*: Soulsby D, Anna LJ, Wallner AS (Eds.), NMR Spectroscopy in the Undergraduate Curriculum: First Year and Organic Chemistry Courses Volume 2. ACS Publications, Washington, p.31-37.
https://doi.org/10.1021/bk-2016-1221.ch003

Mergenthaler P, Lindauer U, Dienel GA, et al., 2013. Sugar for the brain: the role of glucose in physiological and pathological brain function. *Trends Neurosci*, 36(10):587-597.
https://doi.org/10.1016/j.tins.2013.07.001

Milone M, Wong LJ, 2013. Diagnosis of mitochondrial myopathies. *Mol Genet Metab*, 110(1-2):35-41.
https://doi.org/10.1016/j.ymgme.2013.07.007

Mirkes C, Shajan G, Chadzynski G, et al., 2016. ^{31}P CSI of the human brain in healthy subjects and tumor patients at 9.4 T with a three-layered multi-nuclear coil: initial results. *Magn Reson Mater Phys*, 29(3):579-589.
https://doi.org/10.1007/s10334-016-0524-9

Moreno-Sánchez R, Rodríguez-Enríquez S, Marín-Hernández A, et al., 2007. Energy metabolism in tumor cells. *FEBS J*, 274(6):1393-1418.
https://doi.org/10.1111/j.1742-4658.2007.05686.x

Nehrke K, Börnert P, 2012. DREAM—a novel approach for robust, ultrafast, multislice B_1 mapping. *Magn Reson Med*, 68(5):1517-1526.
https://doi.org/10.1002/mrm.24158

O'Donnell ME, Chen YJ, Lam TI, et al., 2013. Intravenous HOE-642 reduces brain edema and Na uptake in the rat permanent middle cerebral artery occlusion model of stroke: evidence for participation of the blood–brain barrier Na/H exchanger. *J Cereb Blood Flow Metab*, 33(2): 225-234.
https://doi.org/10.1038/jcbfm.2012.160

Ren JM, Sherry AD, Malloy CR, 2015. ^{31}P-MRS of healthy human brain: ATP synthesis, metabolite concentrations, pH, and T_1 relaxation times. *NMR Biomed*, 28(11):1455-1462.
https://doi.org/10.1002/nbm.3384

Roach PJ, 2002. Glycogen and its metabolism. *Curr Mol Med*, 2(2):101-120.
https://doi.org/10.2174/1566524024605761

Robbins NM, Swanson RA, 2014. Opposing effects of glucose on stroke and reperfusion injury: acidosis, oxidative stress, and energy metabolism. *Stroke*, 45(6):1881-1886.
https://doi.org/10.1161/STROKEAHA.114.004889

Rothman DL, de Graaf RA, Hyder F, et al., 2019. In vivo ^{13}C and ^{1}H-[^{13}C] MRS studies of neuroenergetics and neurotransmitter cycling, applications to neurological and psychiatric disease and brain cancer. *NMR Biomed*, 32(10): e4172.
https://doi.org/10.1002/nbm.4172

Scheuermann-Freestone M, Madsen PL, Manners D, et al., 2003. Abnormal cardiac and skeletal muscle energy metabolism in patients with type 2 diabetes. *Circulation*, 107(24):3040-3046.
https://doi.org/10.1161/01.CIR.0000072789.89096.10

Shapiro EM, Borthakur A, Dandora R, et al., 2000. Sodium visibility and quantitation in intact bovine articular cartilage using high field ^{23}Na MRI and MRS. *J Magn Reson*, 142(1):24-31.
https://doi.org/10.1006/jmre.1999.1932

Taglang C, Batsios G, Mukherjee J, et al., 2022. Deuterium magnetic resonance spectroscopy enables noninvasive metabolic imaging of tumor burden and response to therapy in low-grade gliomas. *Neuro Oncol*, 24(7):1101-1112. https://doi.org/10.1093/neuonc/noac022

Valkovič L, Chmelík M, Krššák M, 2017. *In-vivo* ^{31}P-MRS of skeletal muscle and liver: a way for non-invasive assessment of their metabolism. *Anal Biochem*, 529:193-215. https://doi.org/10.1016/j.ab.2017.01.018

von Morze C, Engelbach JA, Blazey T, et al., 2021. Comparison of hyperpolarized ^{13}C and non-hyperpolarized deuterium MRI approaches for imaging cerebral glucose metabolism at 4.7 T. *Magn Reson Med*, 85(4):1795-1804. https://doi.org/10.1002/mrm.28612

Warburg O, 1956. On respiratory impairment in cancer cells. *Science*, 124(3215):269-270. https://doi.org/10.1126/science.124.3215.269

Weiss N, Hilaire PBS, Colsch B, et al., 2016. Cerebrospinal fluid metabolomics highlights dysregulation of energy metabolism in overt hepatic encephalopathy. *J Hepatol*, 65(6):1120-1130. https://doi.org/10.1016/j.jhep.2016.07.046

Zhang XT, Zhang Y, Roe AW, 2021. Ultra-high-field MRI studies of brain structure and function in humans and nonhuman primates: a collaborative approach to precision medicine. *Curr Opin Biomed Eng*, 20:100320. https://doi.org/10.1016/j.cobme.2021.100320

Zhang Y, Gao Y, Fang K, et al., 2022. Proton/deuterium magnetic resonance imaging of rodents at 9.4T using birdcage coils. *Bioelectromagnetics*, 43(1):40-46. https://doi.org/10.1002/bem.22382

Supplementary information

Figs. S1–S5; Table S1; Video S1